J. Fluid Mech. (2007), *vol.* 588, *pp.* 253–277.
doi:10.1017/S0022112007007525 Printed in the United Kingdom

The geometric properties of high-Schmidt-number passive scalar iso-surfaces in turbulent boundary layers

L. P. DASI, F. SCHUERG AND D. R. WEBSTER

School of Civil and Environmental Engineering, Georgia Institute of Technology, Atlanta, GA 30332-0355, USA

(Received 7 December 2005 and in revised form 22 May 2007)

The geometric properties are quantified for concentration iso-surfaces of a high-Schmidt-number passive scalar field produced by an iso-kinetic source with an initial finite characteristic length scale released into the inertial layer of fully developed open-channel-flow turbulent boundary layers. The coverage dimension and other measures of two-dimensional transects of the passive scalar iso-surfaces are found to be scale dependent. The coverage dimension is around 1.0 at the order of the Batchelor length scale and based on our data increases in a universal manner to reach a local maximum at a length scale around the Kolmogorov scale. We introduce a new parameter called the coverage length underestimate, which demonstrates universal behaviour in the viscous–convective regime for these data and hence is a potentially useful practical tool for many mixing applications. At larger scales (in the inertial–convective regime), the fractal geometry measures are dependent on the Reynolds number, injection length scale, and concentration threshold of the iso-surfaces. Finally, the lacunarity of the iso-surface structure shows that the instantaneous scalar field is most inhomogenous around the length scale corresponding to the Kolmogorov scale.

1. Introduction

Mixing and transport of passive scalars in turbulent shear flows are important processes occurring in many natural and engineered environments. From a spatial perspective, the instantaneous passive scalar field appears as regions of clear and dyed fluid (or unmixed and mixed fluid). Interfaces between these fluid regions, defined by a scalar threshold value, are typically characterized as convoluted, folded and wrinkled surfaces (e.g. Catrakis 2000). The geometry of the interfacial surface has significant practical importance in a number of applications. First, in non-reactive mixing processes, the molecular diffusive flux occurs across concentration gradients at interfaces (e.g. Sreenivasan *et al.* 1989; Schumacher & Sreenivasan 2005). Estimating the resulting mixing rate is necessary, for example, for predicting the dilution of pollutants into the atmosphere or the discharge of wastewater into a stream. Secondly, in reactive mixing, the reaction rate depends on the size and shape of the interface (e.g. Pope 1988). Examples include combustion chambers in vehicles or power plants and reactors in chemical engineering processes. Thirdly, electromagnetic and acoustic wave propagation in fluids is influenced by interfacial structure (Freund 2001; Fitzgerald & Jumper 2004). Because the wave speed commonly changes across interfaces, passing waves are subject to refraction and reflection. This effect is encountered in aero-optic

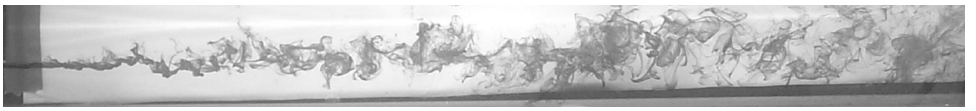

FIGURE 1. Dye visualization of the plume at $Re = 10\,000$ with a nozzle diameter of $D_{nozzle} = 4.7$ mm.

and aero-acoustic applications, for example in earth-based astronomy and for aircraft noise control.

The objective of the current study is to characterize interfacial surfaces of high-Schmidt-number passive scalar fields using fractal geometric measures and examine the relationship between these measures and the large-scale characteristics of the field. The fractal geometry of interfaces in turbulent flows has been investigated since the fundamental suggestions of Welander (1955) and Mandelbrot (1975). Several early papers suggested that the fractal dimension of scalar iso-surfaces was a constant value over the scales of the inertial–convective range (e.g. Sreenivasan & Meneveau 1986; Prasad & Sreenivasan 1990; reviewed by Sreenivasan 1991). In contrast, Miller & Dimotakis (1991) found that the fractal dimension in turbulent jets depended on the spatial scale and concentration threshold. Similarly, Frederiksen, Dahm & Dowling (1996, 1997) showed that for one-dimensional transects, a constant fractal dimension (estimated at 0.48) existed for the viscous–convective range, whereas the dimension depended on scale for length scales larger than the Kolmogorov scale. For planar and three-dimensional transects of the passive scalar iso-surfaces, there was no evidence of a constant fractal dimension. Further, Villermaux & Innocenti (1999) observed that the fractal dimension depends on scale and also varies with time, injection scale and concentration threshold. Table 1 summarizes these studies, including the specific fractal dimension observations.

To describe the fractal geometry of passive scalar iso-surfaces in turbulent jets more fully, Catrakis & Dimotakis (1996, 1998) introduced additional fractal measures, such as the coverage fraction, scale distribution probability density function (PDF), scale-dependent area-volume fraction, and largest empty box (LEB) scale PDF. The fractal dimension was found to be a function of scale for the data collected. A Poisson or log-normal distribution was suggested as a model for the scale distribution PDF. Based on the LEB scale PDF, Catrakis (2000) characterized folding (large-scale process) and wrinkling (small-scale process) via dimensionless numbers for passive scalar iso-surfaces in a turbulent jet.

Although a constant fractal dimension over the inertial–convective regime was initially believed to exist, Catrakis, Aguirre & Ruiz-Plancarte (2002) argued that, unlike the energy spectra, the fractal dimension at a given length scale depends on all larger length scales. Therefore, large-scale anisotropy masks the constant fractal dimension, even if it exists. As an alternative, the scale-local area–volume density was defined to represent better the classical inertial–convective model in physical space. Catrakis *et al.* (2002) found that the area–volume density exhibited self-similarity in the inertial–convective range with a power law exponent of 1.3. Apparently, the area–volume density demonstrated direct manifestations of self-similarity in physical space.

Our objective is to examine the geometry of passive scalar iso-surfaces with respect to the injection length scale (characteristic initial filament size) and Reynolds number. Figure 1 shows an example dye visualization of the studied passive scalar fields. The scalar field shown is a non-buoyant plume introduced iso-kinetically into a turbulent boundary layer. The time-averaged and fluctuating characteristics of similar plumes

Study	Flow	*Re*	Flow scales	Measurement dimensions	Measurement resolution	Scale-dependent coverage dimension?
Sreenivasan & Meneveau (1986)	Boundary layer Axisymmetric jet Plane wake Mixing layer	–	–	–	–	No D in the range 2.32 to 2.40
Sreenivasan *et al.* (1989)	Axisymmetric jet	4000	–	Two spatial dimensions	150 μm × 150 μm × 250 μm	No $D_{ave} = 1.35 \pm 0.05$
Prasad & Sreenivasan (1990)	Axisymmetric jet Cylinder wake	4000 1500	$\eta \approx 150$–160 μm $\eta_B \approx 4$ μm	Dual two spatial dimensions	450 μm × 450 μm × 200 μm	No $D_{ave} = 1.35 \pm 0.05$
Miller & Dimotakis (1991)	Axisymmetric jet	2940–23 400	Smallest scalar scales $\approx \eta \approx 50$–250 μm	Time	80 μm × 80 μm × 80 μm	Yes $0 < D < 1$
Catrakis & Dimotakis (1996)	Axisymmetric jet	4500 9000 18 000	–	Two spatial dimensions	420 μm × 420 μm × 300 μm	Yes $1 < D < 2$
Frederiksen *et al.* (1996)	Axisymmetric jet	3000 3700	Strain-limited estimate of molecular diffusion scale ≈ 257 μm	One dimensional intersections	109 μm × 109 μm × 181 μm	Yes $D_{ave} = 0.48 \pm 0.12$
Frederiksen *et al.* (1997)	Axisymmetric jet	2900 3700 5000	Strain-limited estimate of molecular diffusion scale ≈ 257 μm	Two and three dimensional intersections	110 μm × 110 μm × 181 μm	Yes 2D: $D_{ave} = 1.28$ 3D: $D_{ave} = 2.17$
Villermaux & Innocenti (1999)	Point source in axisymmetric jet	6000	$\eta \approx 100$ μm	Two spatial dimensions	125 μm × 125 μm × 300 μm	Yes
Catrakis *et al.* (2002)	Axisymmetric jet	20000	Smallest scales ≈ 500 μm	Two spatial dimensions + time	Laser sheet thickness = 500 μm	Yes $2 < D < 3$
Present study	Point source in boundary layer	5000 10000 20000	$\eta \approx 290$–760 μm $\eta_B \approx 9$–24 μm	Two spatial dimensions	13 μm × 13 μm × 80 μm	Yes

TABLE 1. Summary of experimental studies of the geometric properties of passive scalar iso-surfaces.

Re	Re_λ	$u^*(\mathrm{mm\,s^{-1}})$	$\eta(\mu\mathrm{m})$	$\eta_B(\mu\mathrm{m})$	$\varepsilon(\mathrm{m^2\,s^{-3}})$	$\mathrm{d}\langle U\rangle/\mathrm{d}y(\mathrm{s^{-1}})$	$u'(\mathrm{mm\,s^{-1}})$
5000	60	3.25	760	24	3.0×10^{-6}	0.18	5.3
10000	90	6.4	420	13	3.3×10^{-5}	0.38	11.8
20000	120	10.6	290	9	1.4×10^{-4}	0.70	19.1

TABLE 2. Flow characteristics. The $\mathrm{d}\langle U\rangle/\mathrm{d}y$ and u' values correspond to the nozzle elevation location. The turbulent kinetic energy dissipation rate was based on scaling estimates of the turbulence intensity and integral length scale. The integral length scale of the velocity and concentration fields were roughly 50 mm and 2 mm, respectively. The Kolmogorov scale was estimated as $\eta \approx (\nu^3/\varepsilon)^{1/4}$, and the Batchelor scale was estimated as $\eta_B \approx (\nu\,\Gamma^2/\varepsilon)^{1/4}$. The Taylor scale was estimated from the isotropic relationship of $\lambda \approx (15\nu u'^2/\varepsilon)^{1/2}$.

have been reported by Fackrell & Robins (1982), Crimaldi, Wiley & Koseff (2002), and Webster, Rahman & Dasi (2003). The local plume structure depends on hydrodynamic conditions, specifically the mean concentration gradient, large-scale intermittency, initial length scale, and Reynolds number. The concentration field produced by a leaky or iso-kinetic release in a turbulent flow is less dense with structure and more intermittent than the field produced by high-momentum jets, which are the subject of many of the studies in table 1. Specifically, the studied fields are sparse and intermittent when the injection length scale is within an order of magnitude of the Kolmogorov scale. Although the influence of the scalar injection length scale has been studied in the context of the cascade-bypass phenomenon (Villermaux, Innocenti & Duplat 2001), its effect on the geometry of concentration iso-surfaces is not established and is a focus of this study.

2. Experiment and flow description

The scalar field was measured downstream of a continuous iso-kinetic nozzle release of Rhodamine 6G solution, a high-Schmidt-number passive scalar ($Sc \approx 1250$; Crimaldi & Koseff 2001), into the inertial layer of a turbulent boundary layer. The resulting scalar field was statistically stationary in time and possessed spatial gradients of both the mean concentration and velocity fields. The flow was a gravity-driven turbulent uniform-depth open-channel flow in a 24.4 m long and 1.07 m wide rectangular channel tilting flume with a smooth bed. Water was supplied to the flume head box from the laboratory constant-head tank. The head box of the flume contained stilling devices (i.e. a wood baffle and two expanded-metal screens covered with a synthetic geotechnical fabric) to minimize large-scale flow perturbations. The resulting flow entering the channel was laterally uniform with low turbulence intensity and minimal surface perturbation.

Experiments were conducted for three Reynolds numbers of 5000, 10 000 and 20 000 based on the bulk velocity and flow depth (see table 2). For each case, the bed slope and the height of the tailgate were adjusted to create an open-channel flow of depth 100 mm (uniform to within $\pm$0.3 mm for 15 m upstream of the measurement location). The boundary layer was fully developed at the measurement location, which was 23 m downstream of the inlet.

Detailed velocity measurements were obtained via particle tracking velocimetry (PTV) (method described in Dasi 2004). For each Reynolds number, the mean velocity and turbulent stress characteristics agreed well with previous turbulent boundary-layer studies (figure 2). The wall shear velocities, u^*, were 3.25, 6.4 and 10.6 mm s^{-1} for the respective Reynolds-number cases. The normalized mean velocity profiles agreed well

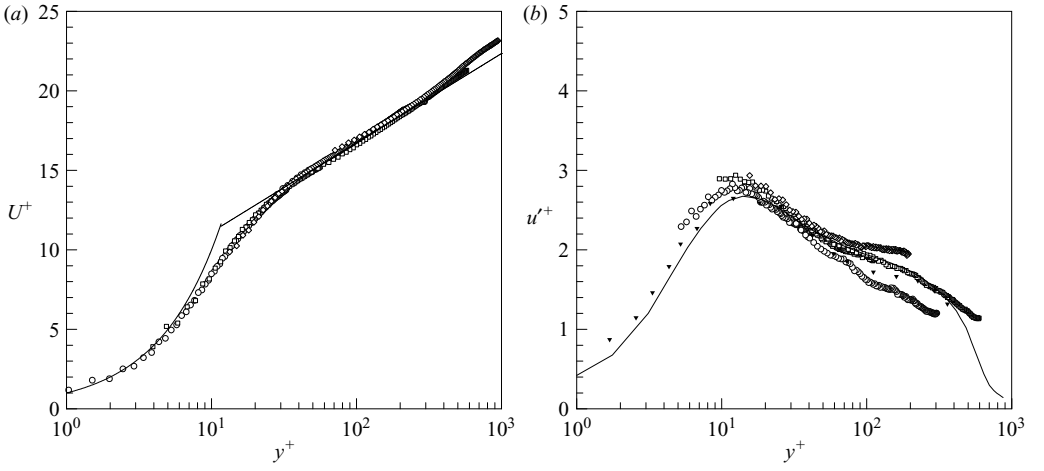

FIGURE 2. Profiles of the normalized (*a*) mean and (*b*) root mean square of the streamwise velocity for $Re = 5000$ (○); 10 000 (□); 20 000 (◇). The momentum thickness Reynolds numbers are 540, 1200 and 1880, respectively. The solid line in (*a*) indicates the viscous sublayer ($u^+ = y^+$) and log layer ($u^+ = (1/\kappa)\ln\, y^+ + C$, $\kappa = 0.41$, $C = 5.5$) profiles. In (*b*), the data are compared with the experimental data by Tachie *et al.* (2003) (▼) for $Re_\theta = 1450$ and the DNS data by Spalart (1988) (——) for $Re_\theta = 1410$.

with the viscous sublayer, buffer layer and logarithmic layer. The Reynolds stress profiles also agreed well with measurements of Tachie, Balachandar & Bergstrom (2003) and DNS results of Spalart (1988) for similar Re_θ (figure 2).

The plume was released through a brass nozzle aligned with the centreline of the flume and pointed in the downstream direction parallel to the flume bed. Three brass nozzles were employed with inner orifice diameters of $D_{nozzle} = 2.2$, 4.7 and 9.4 mm to study the effect of the initial length scale. The centre of each nozzle orifice was at an elevation of 50 mm above the flume bed. To minimize the wake perturbation, each nozzle was custom-built with a streamlined fairing. The release velocity matched the ambient flow to produce an iso-kinetic release. In this manner, the mixing process was decoupled from the evolution of the velocity field, and in this regard the current study is most similar to that of Villermaux & Innocenti (1999).

Figure 3 shows the schematic of the experimental set-up for the high-resolution planar laser-induced fluorescence (PLIF) technique used to measure the passive scalar field. A laser sheet in the vertical plane along the centreline of the flume was created via scanning mirrors. The laser source was an argon-ion laser (5 W) with a wavelength of 514 nm. A combination of a 6× beam expander and 2 m focal length lens focused the beam to a $1/e^2$ waist diameter equal to 80 μm at an elevation of 50 mm above the flume bed (corresponding to the mid-depth of the flow). The Rayleigh length corresponding to this configuration was 20 mm. Thus, the beam waist was approximately 80 μm throughout the image region. Although the beam waist exceeded the Batchelor length scale (table 2), it was confirmed via spectral analysis of the LIF images that the resolution affected the spectral energy for higher wavenumbers, whereas the mid-range of the viscous–convective regime was resolved (Dasi 2004). A clear 190 mm × 100 mm Plexiglas sheet was suspended just above the water surface with the lower surface wetted to allow the laser beam to enter the measurement region without optical distortion due to small water surface perturbations. The Plexiglas sheet made contact with the water surface only by surface tensile forces. The scanning

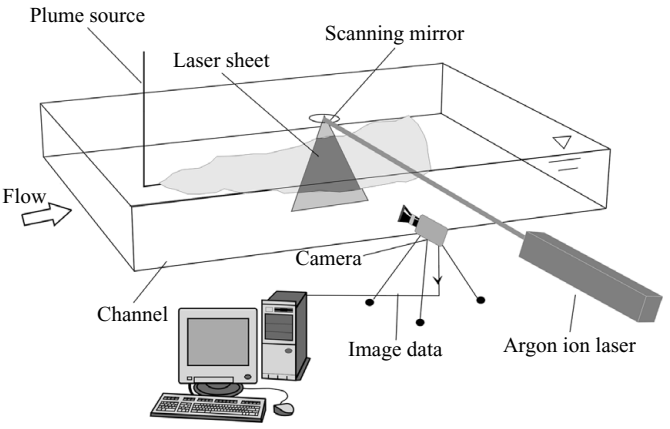

FIGURE 3. Schematic of the experiment set-up for concentration measurements via planar laser-induced fluorescence (PLIF).

mirror system consisted of two mirrors, each mounted on a galvanometer (Cambridge Technology) positioned above the water surface. The voltage signal that controlled the mirror position was generated by a National Instruments multifunction input/output board. The scan time of 3 ms ensured sufficient illumination of the tracer field while minimizing the horizontal distortion of the dye filaments due to advection to less than 3 % for the fastest flow $Re = 20000$). The distortion was less for the slower-flow cases with a maximum of 1.5 % and 0.75 % for $Re = 10\,000$ and 5000, respectively.

The image acquisition camera was a 12-bit CCD camera with 1392×1024 pixels (LaVision). A 200 mm Nikon MicroNikkor macro lens was used to provide a magnification of approximately 13 μm/pixel, which nearly matches the Batchelor length scale at the largest Reynolds number. The image field covered approximately 18 mm × 13 mm in the vertical laser sheet plane along the nozzle centreline. The data collection was conducted at a rate of 10 f.p.s. For each data record, 12 000 consecutive images were captured. Data were collected at six downstream distances from the source: H, $2.5H$, $5H$, $10H$, $20H$ and $40H$, where $H = 100$ mm is the flow depth.

Calibration involved capturing a series of images for uniform concentration fields in the range 0–100 $\mu g\,l^{-1}$. The average intensity was calculated for each pixel from 200 realizations, and the field was corrected for laser attenuation due to the presence of Rhodamine 6G (Ferrier, Funk & Roberts 1993). A least-squares regression yielded the calibration relationship for each individual pixel. Concentration measurement uncertainty resulted from errors in the concentration of the calibration fluid and errors due to digitization by the camera. Combining these considerations yielded a bound on the error for the concentration measurements of ± 4 %. This is a conservative estimate that most directly relates to lower concentration values, whereas higher concentration measurements had a lower uncertainty.

Figure 4 shows two samples of the high resolution concentration fields. In general, the passive scalar field evolved owing to the stretching and folding action of the fluctuating velocity field. The filament of dye was advected downstream by the mean flow, while being dispersed in all directions by the velocity fluctuations. The scalar field thus generated was continuously–connected and only appeared as disconnected sheets in the measured two-dimensional transects of the field. The effect of molecular diffusion played a minimal role in the development of the large-scale plume structure. However, molecular diffusion was critically important to the mixing process because

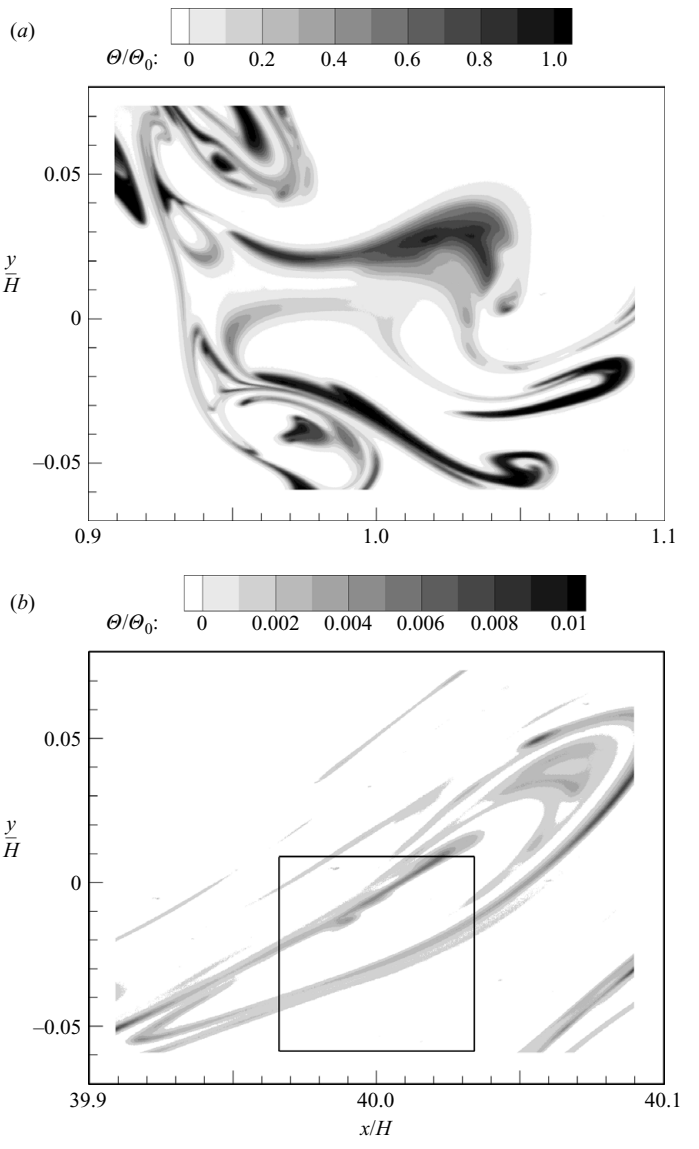

FIGURE 4. Sample concentration fields at (*a*) $x = H$ and (*b*) $40\,H$. Data shown for $Re = 10\,000$ and $D_{nozzle} = 4.7$ mm.

it acted to dilute the filament concentration locally and limited the development of structure below the Batchelor length scale. The sparse filament structure shown in figure 4 is qualitatively different from that observed for turbulent jets (e.g. Villermaux & Innocenti 1999; Catrakis 2000). For the case of turbulent jets, clear fluid was entrained into the initially homogenous jet core, which led to less sparse (and less intermittent) concentration fields.

3. Data analysis

Concentration iso-surfaces for defined threshold levels were extracted for the 512 × 512 pixel array near the centre of the image (figure 4*b*) using the boundary

outline pixel methodology. This sub-region (bounding box) was analysed because the mean concentration gradient ($\partial\langle\Theta\rangle/\partial y$) was constant in this region of the field. The uniform mean concentration gradient region was preferred to ensure that large-scale characteristics of the concentration field are uniform throughout the bounding box. Concentration iso-surfaces corresponding to three thresholds were extracted for each image. The threshold concentration, $\Theta_{th}(m)$, corresponds to m times the local concentration standard deviation above the local mean concentration (i.e. $\Theta_{th}(m) = \langle\Theta\rangle + m\langle\theta^2\rangle^{1/2}$), where m was chosen to be 3, 5 and 7. The local mean corresponds to the ensemble average of 12 000 realizations of the spatially averaged value for the bounding box region. The range of concentration thresholds was bounded owing to noise and limited sample size of the data sets. Because of the intermittent nature of the plume, the local mean concentration was orders of magnitude lower than the peak instantaneous concentration. The signal-to-noise ratio of pixel intensities corresponding to concentrations lower than the local mean were poor and therefore limited the range of thresholds to be greater than the mean concentration. Also, for $m > 7$, only a small number of images contained an iso-surface, which prevented statistically converged measures.

Schuerg (2003) tested several iso-surface extraction methods and concluded that the boundary-outline pixel approach is the superior method. A primary advantage of the boundary-outline pixel method is that it eliminates the asymmetry between identifying 'islands' and 'lakes' in the field. The methodology considered the concentration of a pixel (called the 'centre pixel'). If the concentration of the centre pixel was greater than or equal to the threshold concentration, then the surrounding eight pixels were examined for threshold crossings. A neighbouring pixel with a concentration below the threshold indicated a crossing between that pixel and the centre pixel. A linear interpolation of the concentration between the two pixels was used to calculate the location of the crossing. The pixel closest to the crossing was flagged as a boundary outline pixel. If the location was exactly halfway between the two pixels, then both pixels were flagged as the boundary outline pixel. This methodology was used for every pixel in each image to generate the iso-surface for the defined concentration threshold. The outcome was a binary image consisting of the iso-surface.

Figure 5 provides a qualitative picture of the temporal and spatial evolution of the passive scalar iso-surfaces. The figure corresponds to the iso-surfaces extracted from 16 consecutive images for the concentration threshold $\Theta_{th}(m) = \langle\Theta\rangle + \langle\theta^2\rangle^{1/2}$ (i.e. $m = 1$ for demonstration) at the farthest downstream distance for the case of $Re = 10\,000$ and $D_{nozzle} = 4.7\,\text{mm}$. Note that figure 5(vii) corresponds to the field shown in figure 4(*b*). Although not shown here, the scalar structure appears to be more stretched and thinner as distance from the source is increased. The iso-surfaces appear randomly located in space and time with a shape that is impossible to describe with traditional tools of Euclidian geometry. Also, the iso-surfaces generally occupy only a small portion of the bounding box. The convoluted nature of the iso-surfaces represents structure over a large range of scales from the Batchelor scale to the scale of the bounding box. The scalar iso-surfaces possess structure at larger scales, but we examine only the geometry within the equilibrium range (i.e. from the Batchelor scale to the inertial–convective range). Another important observation is that the iso-surface structure is visually unlike the passive scalar iso-surfaces generated by a high-momentum jet (e.g. Catrakis & Dimotakis 1996). The iso-surface structure in the present study is sparse without obvious whorls or saddle structures.

The box-counting algorithm was applied to a boundary-outline pixel image and extracted values of the coverage count as a function of length scale, λ. The algorithm

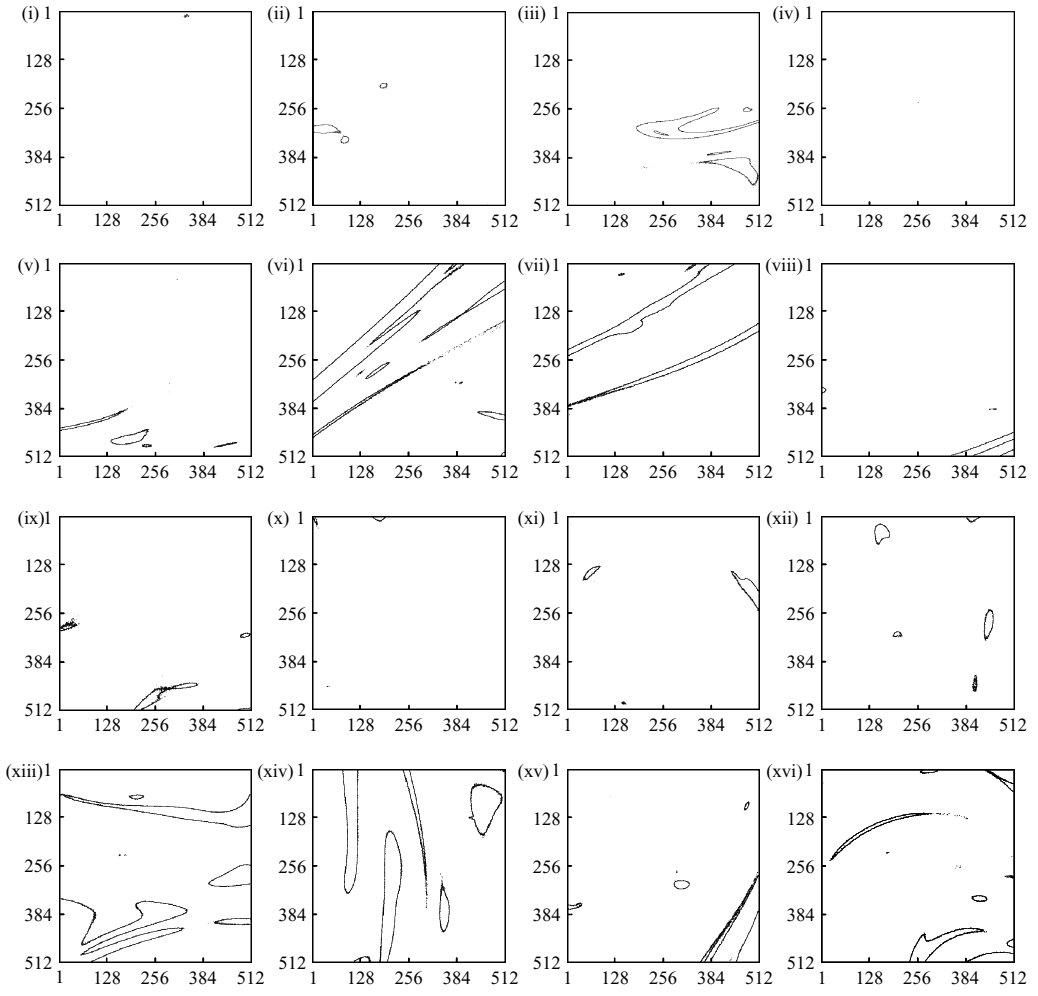

FIGURE 5. The first 16 consecutive samples from the set of 12 000 boundary-outline images at $x = 40\,H$ for a concentration threshold of $\Theta_{th}(m) = \langle\Theta\rangle + m\langle\theta^2\rangle^{1/2}$, where $m = 1$ for demonstration. For every image the streamwise direction is from left to right.

started with a bounding box with a characteristic side scale, δ_b, defining the largest considered scale. The bounding box was successively subdivided into an increasing number of boxes of smaller size, until the boxes reached pixel size; hence the consecutive box sizes were $\lambda = 512$, 256, 128, 64, 32, 16, 8, 4, 2 and 1 pixels. At each subdivision step, the algorithm counted the number of boxes that contain part of the iso-surface, which yielded the coverage count, $N(\lambda)$, at the particular length scale. Following the recommendation of Miller & Dimotakis (1991), the starting position of the subdivision was shifted to eight starting locations in each coordinate direction. Thus, for each box size, λ, we shifted the grid to $8 \times 8 = 64$ different locations. For the smallest scale of 1 pixel, only one position with the shifting grid was possible. For the second-smallest subdividing box, there were $2 \times 2 = 4$ possible shifting positions, and so on. Of course, it does not make sense to shift the grid for the largest length scale. Some boxes shifted past the boundaries of the image. In such circumstances, we artificially connected the left-hand image boundary to the right-hand one, and

the upper image boundary to the lower one. As discussed in the next section, other fractal measures were calculated based on the coverage count results. The results were ensemble-averaged over the full record of images.

There is an important issue associated with applying the box-counting algorithm owing to the sparseness of the iso-surface structure. When ensemble-averaging over a number of images, completely empty images decreased the coverage count, but did not contribute any information for the coverage dimension. One option was to exclude such images from the ensemble calculations. As the bounding box size was an arbitrary length scale within the field, we could argue that smaller empty regions within the images should also be left unconsidered. One way to do this was to neglect the coverage count of images down to length scales where the iso-surface structure occupied more than one of the subdividing boxes. This corresponded to an adaptation of the bounding box to the largest iso-surface structure present within a particular image. We investigated the impact of rejecting empty regions on the various fractal measures. On the one hand, this approach seemed to improve the performance of the algorithm in reproducing the exact fractal dimension of synthetic objects (discussed below). On the other hand, it discarded an essential characteristic of the flow field, i.e. the sparseness of the iso-surface structure. We concluded that the physics of the field were represented most accurately when the empty regions were included. Thus, we consistently used the full size of the initial bounding box.

Before analysing the fractal characteristics of the passive scalar iso-surfaces, it was necessary to validate the numerical method by evaluating the performance when applied to deterministic self-similar fractal objects of known theoretical dimension. This is particularly true for the current data set in which the largest scales in the field were much larger than our bounding box. We created fractal objects with the same range of scales, and extracted 512×512-pixel-sized images from these objects. In addition to general validation of the numerical method, the evaluation image sets allowed us to investigate the influence of several parameters on the algorithm accuracy, such as the dimension, the number of shifts of the starting location, and the adaptation of the bounding box.

Based on the examples of classical and detached Koch curves given by Mandelbrot (1983), we developed six deterministic fractals with the dimensions $D \approx 1.0000$, 1.1046, 1.2553, 1.4466, 1.6131 and 1.7604. The deterministic self-similar fractals were created by performing the same prescribed operation (called the 'generator') repeatedly on a starting object (called the 'initiator'). In each case, a square was used as the initiator. To introduce irregularity and asymmetry in the resulting fractal objects with varying numbers of detached islands and lakes, we randomly picked generators from a set with the same cumulative fractal dimension, but varying degrees of dispersion (Schuerg 2003). We matched the order of the desired scaling by selecting the proper level of the self-similar cascade, i.e. the number of times the generator was applied. In order to apply our algorithm to the deterministic fractal objects, it was necessary to create boundary-outline pixel images from the array of straight lines. We first rotated the whole fractal object by a random angle, which eliminated alignment of the box-counting subdivisions and the object. The rotated object was scaled to fit the resolution requirement at the smallest scale. Then, a selector square of the size of our images (i.e. 512×512 pixels) was randomly located within the fractal object. The part of the object lying within the selector square was used to create one boundary-outline pixel image. For each of the six dimension cases, we created 1200 random objects and extracted 10 images from each realization. Thus, a total of 12 000 evaluation images were created for each case. While there are clear differences from the turbulence

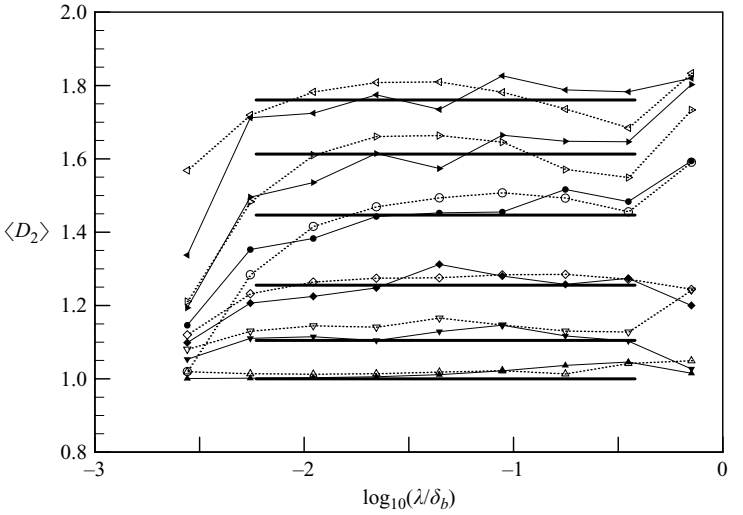

FIGURE 6. Coverage dimension calculated via the numerical method for the Koch curve objects (closed symbols) and fBm objects (open symbols). The theoretical fractal dimension is indicated by the thick horizontal lines over the range in which the algorithm accuracy is to be evaluated.

data because of the deterministic nature of the Koch curve test images, there are general similarities regarding the sparseness of the fields, the arbitrary location and orientation of the interface structure, and the fact that the interface structure extends beyond the edge of the bounding box.

In addition, we created simulated concentration contours based on fractional Brownian motion (fBm) and generated random evaluation sets with the same six fractal dimensions as the Koch curves. The fBm sets were created via simulating two-dimensional Brownian motion by implementing the random mid-point displacement method (Peitgen, Jürgens & Saupe 1992). By adjusting the Hurst exponent, which may vary from 0 to 1, fBm sets were produced with the desired fractal dimension. From each fBm object, the bounding curve of the object was extracted as the representative fBm generated iso-surface. For each of the six dimension cases, we created 12 000 random fBm objects. A randomly located 512×512 pixel bounding box region was extracted from each object image for analysis. In addition to testing the code, results of the analysis of the randomly generated fBm objects were compared to the parameters calculated for the turbulent scalar iso-surfaces.

Figure 6 shows the coverage dimension for the Koch and fBm evaluation image sets for six fractal dimensions. For intermediate scales, the data show a plateau matching the theoretical dimension. The algorithm performs well on fBm sets and Koch curves. However, fluctuations around the correct value are evident along each plateau. According to Sreenivasan (1991), these fluctuations originate from two sources. First, the dyadic subdivision factor of the box-counting algorithm (i.e. 1/2) generally does not correspond to the intrinsic subdivision factor of a particular Koch curve determined by its generator or the more random fBm objects. Secondly, the starting location of the subdivision usually does not match the starting points of straight-line elements of the Koch curve. Errors at the boundaries of the algorithm scaling range were reported in the literature (e.g. Miller & Dimotakis 1991; Shepherd, Cheng & Talbot 1992; Frederiksen *et al.* 1996), which is consistent with the deviation at the smallest and largest scales shown in figure 6. For the current simulated data, the

error in the numerically determined dimension averaged over the 7-point plateau was less than 1 %. The fluctuation root mean square for those points about the expected value was less than 5 %. Tests with these simulated images also revealed that eight shifting locations for the start of the box-counting algorithm is the optimal balance of benefit and computational cost. The approach of artificially connecting the left and right boundaries for subdivided boxes that extend past the edge was found to be superior to weighting and other schemes.

Error analysis was also performed based on the statistical behaviour of the turbulent data set. The standard error of the ensemble average of the coverage count data was calculated based on the standard deviation and number of samples. The estimate of the standard error subsequently was propagated to all quantities that depend on the coverage count. Since the lacunarity (another geometric parameter discussed) does not follow from the coverage count, the standard error was calculated directly from the ensemble of data. For each individual data point shown in figures 7–16, error analysis was performed and error bars are shown. The worst case for the standard error in coverage dimension was 6 % and for the standard error in coverage length underestimate was 4 %.

4. Results based on the coverage count

This section describes the scalar iso-surfaces quantitatively with respect to the coverage statistics. The primary focus is on the effects of concentration threshold, velocity characteristics (governed by Reynolds number of the boundary-layer flow), mean scalar characteristics (governed by distance from the source), and injection length scale (nozzle diameter) on these measures.

The coverage count, at a given scale λ, is the number of boxes of size λ in the grid that contain part of the scalar iso-surface within the bounding box. There are a number of other measures based on the coverage count that yield a comprehensive description of the fractal geometry of the iso-surfaces. These measures are collectively called the coverage statistics, of which Catrakis & Bond (2000) provided a valuable overview.

All of the measures in the coverage statistics are based on the discrete coverage count, $N_2(\lambda)$, generated by the box-counting algorithm. The subscript indicates the embedding dimension, $d = 2$ for our planar measurements. Figure 7 shows a typical coverage count plot for the three threshold levels. The coverage count decreases with λ and threshold level. These trends agree with the numerical simulations of isotropic turbulence reported by Schumacher & Sreenivasan (2005). Further, the variation with respect to threshold level is consistent with Miller & Dimotakis (1991) and Villermaux & Innocenti (1999) for passive scalar mixing in a jet. Also, the coverage count at $\lambda = \delta_b$ is not necessarily unity and decreases with increasing threshold because of the presence of empty bounding boxes. As the scale size increases and crosses over the Kolmogorov scale (at $\log_{10}(\lambda/\delta_b) \approx -1.2$), the negative slope of the coverage count distribution appears to reduce in magnitude.

The coverage dimension or box-counting dimension, defined as the logarithmic derivative of the coverage count of the object, is given by:

$$D_d(\lambda) = -\frac{\mathrm{d}\log N_d(\lambda)}{\mathrm{d}\log \lambda}. \tag{4.1}$$

Although the coverage dimension is not equal to the more accurate Hausdorff–Besicovitch dimension even for simple deterministic self-similar fractals, the literature

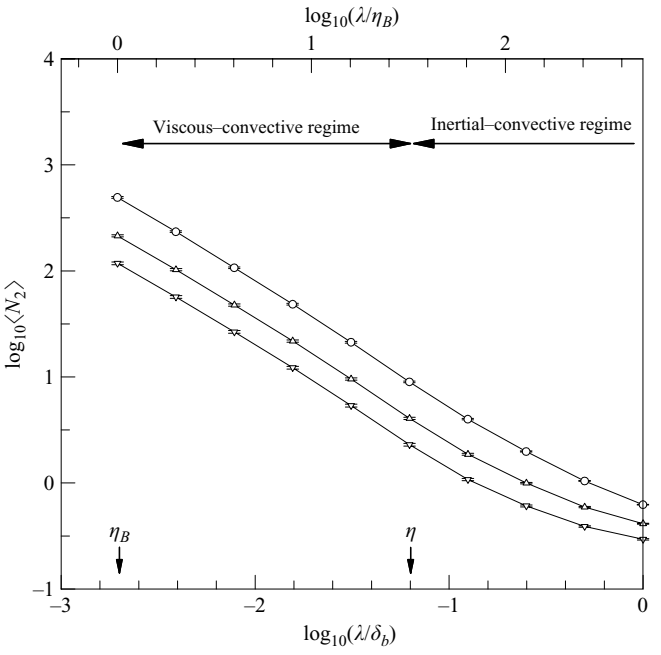

FIGURE 7. Coverage count as a function of concentration threshold. Data plotted versus normalized scales, λ/δ_b and λ/η_B, for the passive scalar iso-surface at a concentration m times the local standard deviation above the local mean, for $m = 3$ (○), 5 (△) and 7 (▽), at $x = 40\,H$; for $D_{nozzle} = 4.7$ mm and $Re = 10\,000$.

mentioned in § 1, for instance, showed that it successfully captures most characteristics of fractal objects. Equation (4.1) was implemented by central differencing.

As reported in § 1, contradicting observations exist regarding the coverage dimension of the passive scalar iso-surfaces. Sreenivasan & Meneveau (1986) observed a constant fractal dimension with respect to scale size, whereas Catrakis & Dimotakis (1996) and others observed a scale-dependent fractal dimension implying a level 3 complexity (i.e. scale dependence, as defined in Catrakis & Dimotakis 1996) of the iso-surfaces. For reference, table 1 summarizes the coverage dimension observations of several recent studies. Figure 8 shows the variation of the coverage dimension with respect to the concentration thresholds applied to the passive scalar field. The coverage dimension is scale dependent, irrespective of threshold, in contrast to figure 6 for the synthetic objects. The scale-dependent coverage dimension characteristic is in agreement with many of the studies summarized in table 1. The coverage dimension for all thresholds increases with scale in the viscous–convective range, $-2.7 < \log_{10}(\lambda/\delta_b) < -1.2$, indicating that the convolution of the iso-surfaces appears to be more space filling. Also, the coverage dimension is less sensitive to variations in the concentration threshold; the coverage dimension appears to be the same for the three concentration thresholds. The majority of measurements in table 1 did not resolve the viscous–convective regime, and hence it is impossible to assess whether the trend observed in the current data is common to other flow geometries.

The profiles at scales larger than the Kolmogorov length scale, in contrast, are sensitive to variations in the concentration threshold. Specifically, the coverage dimension decreases with increasing concentration threshold. The decrease in coverage dimension occurs because at scales larger than the Kolmogorov scale, the iso-surfaces

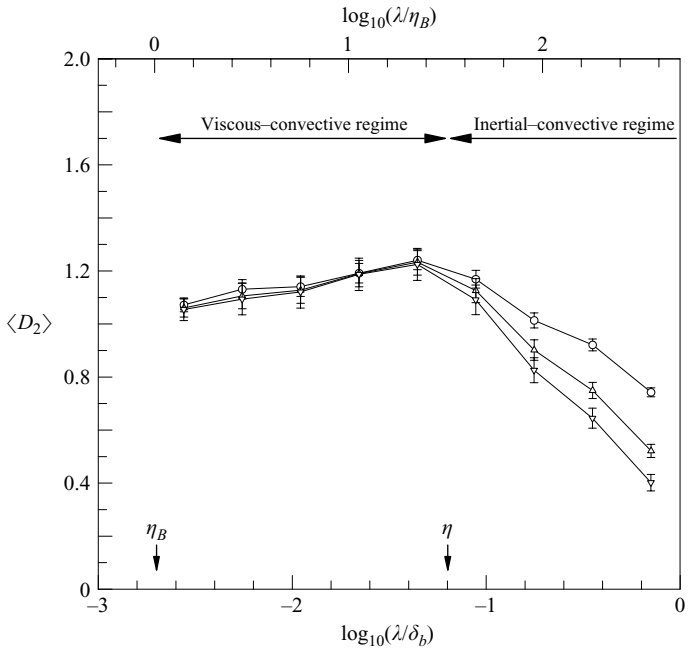

FIGURE 8. Coverage dimension as a function of concentration threshold. Data plotted versus normalized scales, λ/δ_b and λ/η_B, for the passive scalar iso-surface at a concentration m times the local standard deviation above the local mean, for $m = 3$ (○), 5 (△) and 7 (▽), at $x = 40\,H$; for $D_{nozzle} = 4.7$ mm and $Re = 10\,000$.

are often completely inside the λ-sized box, thereby appearing as a collection of spots. Unlike previous observations in which the bounding box covers the entire jet flow structure, the iso-surfaces appear more and more 'spotty' ($D_2 < 1$) as the size of the boxes increases. Hence, the sparseness of the structure, especially for the larger threshold values, leads to the observed trend for coverage dimension in the inertial–convective range.

Figure 9 shows the variation of the coverage dimension with increasing distance from the source for different concentration threshold levels. The coverage dimension in the viscous–convective regime is nearly independent of downstream distance from the source. Therefore, the coverage dimension in the viscous–convective regime is not dependent on concentration threshold or any global characteristic of the scalar field dependent on the downstream distance, such as the mean scalar gradient.

For scale sizes larger than the Kolmogorov length scale, the coverage dimension varies with the global characteristics of the mean scalar field. The coverage dimension in the inertial–convective regime decreases with increasing distance from the source. This indicates that the iso-surfaces become more sparse with fewer clusters of structure that tend to increase the coverage dimension. Also, the coverage dimension curves in the inertial–convective regime for the far downstream cases vary little with distance. Most of the variation occurs for $x < 10H$, suggesting that a constant state is reached such that the characteristics of the geometry of the iso-surfaces are fixed in the inertial–convective regime for $x > 10H$.

Figure 10 shows the variation of coverage dimension with Reynolds number. In the viscous–convective regime, the coverage dimension appears to be independent of Reynolds number, except for the lowest Reynolds number where the curve is flatter

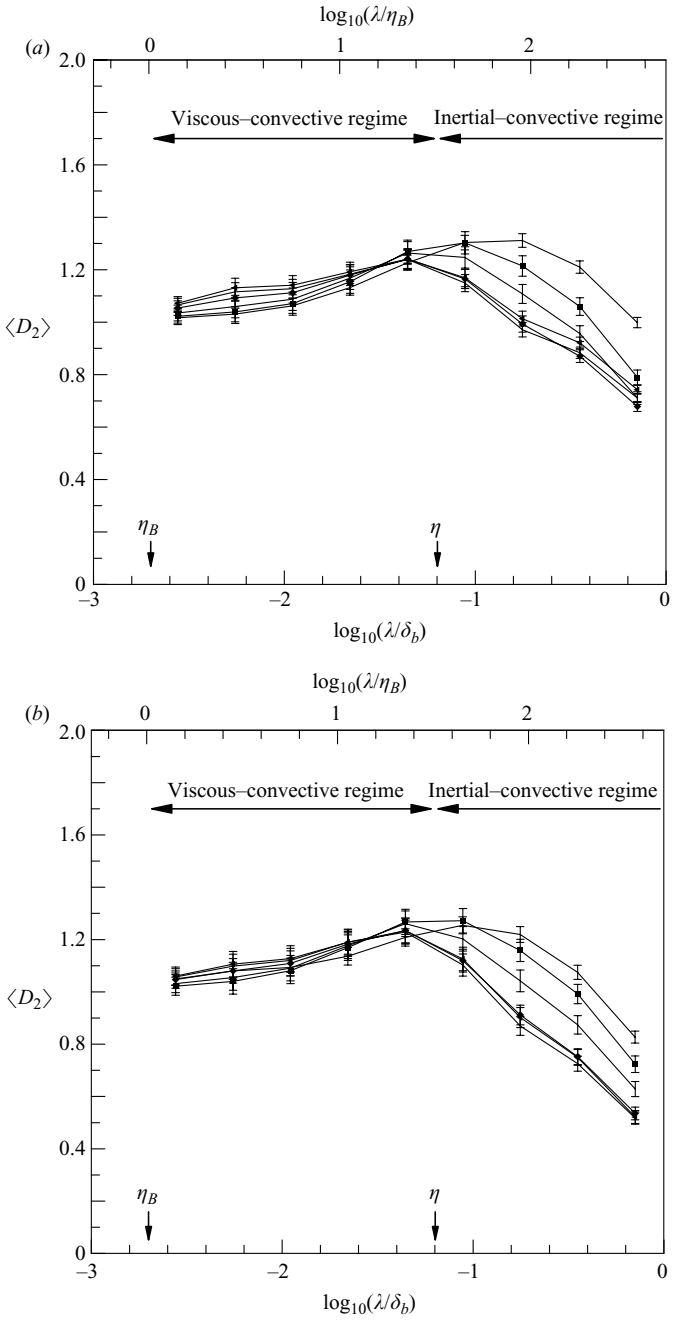

FIGURE 9(*a*, *b*). For caption see next page.

than those for higher Reynolds numbers. It can be concluded that the coverage dimension in the viscous–convective range behaves in a universal manner even for moderately high Reynolds numbers ($Re \geqslant 10\,000$). Note that this value is consistent with the mixing transition identified by Dimotakis (2000) for shear layers, jets and other flows. In the inertial–convective range, the coverage dimension for the lowest Reynolds number is significantly lower than the other cases. This Reynolds-number

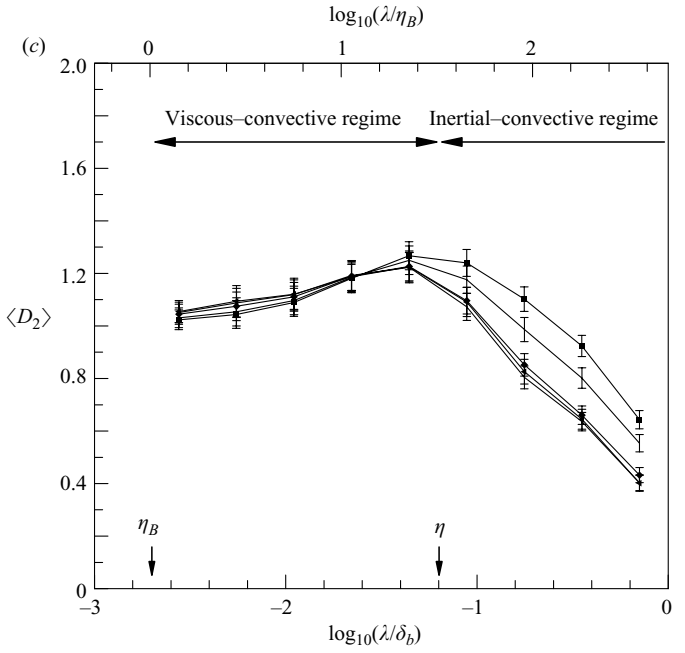

FIGURE 9. Coverage dimension as a function of distance from the source. Data plotted versus normalized scales, λ/δ_b and λ/η_B, for the passive scalar iso-surface at a concentration m times the local standard deviation above the local mean, for (*a*) $m = 3$, (*b*) 5 and (*c*) 7, at $x = H$ ($\triangledown$), $2.5\,H$ ($\blacksquare$), $5\,H$ ($\triangle$), $10\,H$ ($\blacklozenge$), $20\,H$ ($\bigcirc$), and $40\,H$ ($\blacktriangleleft$); for $D_{nozzle} = 4.7$ mm and $Re = 10\,000$.

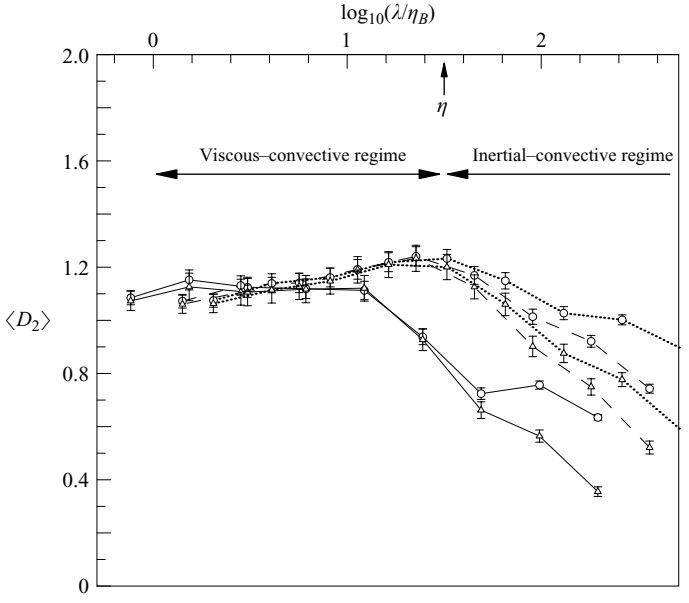

FIGURE 10. Coverage dimension as a function of Reynolds number. Data plotted versus normalized scale, λ/η_B, for the passive scalar iso-surface at a concentration m times the local standard deviation above the local mean, for $m = 3$ ($\bigcirc$) and 5 ($\triangle$), at $x = 40\,H$; for $D_{nozzle} = 4.7$ mm and $Re = 5000$ (——), 10 000 (– – –) and 20 000 ($\cdots$).

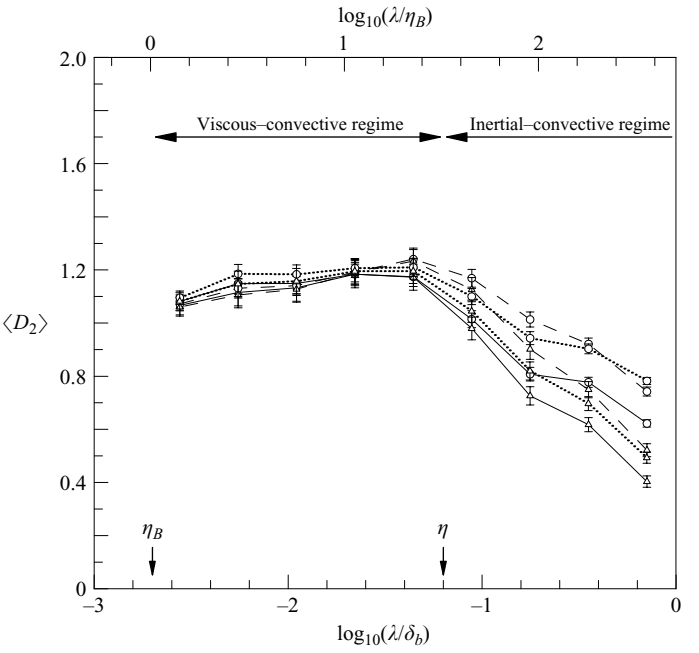

FIGURE 11. Coverage dimension as a function of source nozzle diameter. Data plotted versus normalized scales, λ/δ_b and λ/η_B, for the passive scalar iso-surface at a concentration m times the local standard deviation above the local mean, for $m = 3$ (○) and 5 (△), at $x = 40\,H$; for $D_{nozzle} = 2.2$ mm (——), 4.7 mm (– – –) and 9.4 mm (· · ·) and $Re = 10\,000$.

dependence may be explained from the fact that the intermittency factor increases with Reynolds number (Dasi 2004). This implies that the scalar field is less sparse for higher Reynolds number, thereby increasing the coverage dimension. Note that the coverage dimension remains below 1 in the inertial–convective range for the range of Reynolds number. For higher Reynolds number, the coverage dimension in this range may exceed 1, which would indicate that the iso-surfaces, although sparse, have smoother large-scale structures.

Figure 11 shows the variation of coverage dimension with nozzle diameter. Again, the universal behaviour in the viscous–convective regime is evident. In the inertial-convective regime, the coverage dimension is lowest for $D_{nozzle} = 2.2$ mm and highest for $D_{nozzle} = 4.7$ mm. Because of the non-monotonic trend with nozzle size, factors besides intermittency appear to influence the coverage dimension. Possible influences include the shape of the PDF of the concentration fluctuations, which also demonstrates a non-monotonic trend with nozzle diameter (Dasi 2004), and the relative size of the release nozzle compared to the Taylor scale. In this case, the Taylor length scale corresponds to a scale between the diameters of the middle-sized and largest nozzles, which may lead to a fundamental shift in the mixing characteristics (see Lück *et al.* 2006).

The coverage length, $L_d(\lambda)$, measures the total length of the iso-surface in the bounding box using a ruler of size λ. For the present case with $d = 2$, this measure corresponds to the length of the interface boundary for the scalar field measured. This measure is calculated as:

$$L_d(\lambda) = \lambda^{d_t} N_d(\lambda), \tag{4.2}$$

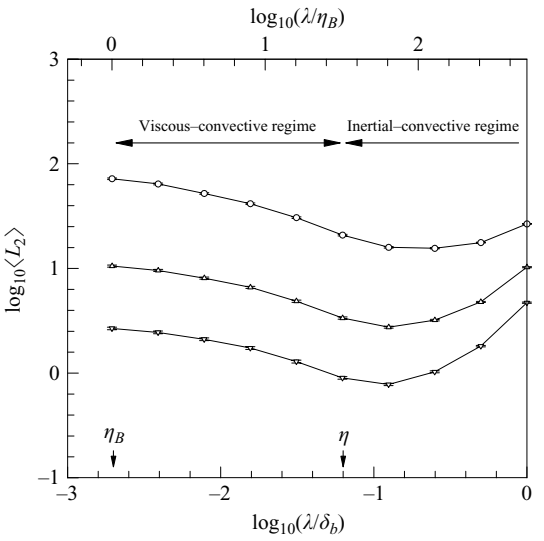

FIGURE 12. Coverage length as a function of concentration threshold. Data plotted versus normalized scales, λ/δ_b and λ/η_B, for the passive scalar iso-surface at a concentration m times the local standard deviation above the local mean, for $x = 3$ (○), 5 (△) and 7 (▽), at $x = 40\,H$; for $D = 4.7$ mm and $Re = 10\,000$.

where d_t is the topological dimension of the set and is equal to 1 for our measurements. Note that $L_d(\lambda)$ tends to the total coverage length, $L_{d,tot}$, as $\lambda \to 0$. For classical fractal objects, the total coverage length is infinity owing to self-similarity at arbitrarily small scales. For the passive scalar field, no additional fine structure exists in the iso-surface for $\lambda < \eta_B$, which results in no change in $L_d(\lambda)$.

From a turbulent mixing application point of view, the coverage area $L_3(\lambda)$ is the most important measure of iso-surfaces because it measures the total interfacial area of iso-surfaces. Therefore, this measure is useful for predicting mixing efficiency or the kinetics of reactive mixing. The coverage length, $\langle L_2(\lambda)\rangle$, measures the average total iso-surface length per bounding box size, δ_b, and hence is the lower dimensional analogue. Figure 12 shows the coverage length in millimetres per bounding box for different concentration thresholds. In the viscous–convective regime, the coverage length decreases with increasing scale and the curves corresponding to different thresholds appear nearly parallel. Above the Kolmogorov length scale, the curves attain a local minima followed by an increase in coverage length. The increase with increasing scale size is possible as the coverage dimension at these scales falls below unity. Overall, the coverage length decreases with increasing threshold. This decrease with increasing threshold can be explained in analogy to the contour lines of 'tapered peaks or hills' of concentration. Increasing the threshold moves the contour up the hill while reducing the perimeter of the contour. Notice that as $\lambda \to \eta_B$, the coverage length of each curve appears to be bounded (i.e. the slope of the $\log_{10}\langle L_2(\lambda)\rangle$ distribution flattens as $\lambda \to \eta_B$). This upper bound is the true length of the iso-surfaces whereas the lengths measured at higher scales may be interpreted as artefacts of lower resolution.

A new coverage measure, namely the coverage length underestimate, is defined here as:

$$\langle L_{2,u}(\lambda/\delta_b)\rangle = \frac{\langle L_{2,tot}\rangle}{\langle L_2(\lambda/\delta_b)\rangle}. \tag{4.3}$$

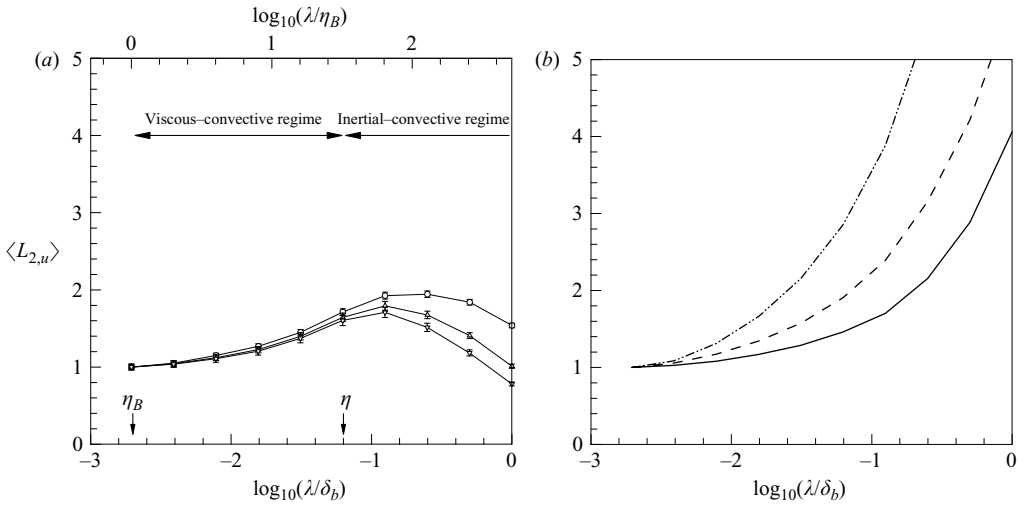

FIGURE 13. (*a*) Coverage length underestimate as a function of concentration threshold. Data plotted versus normalized scales, λ/δ_b and λ/η_B, for the passive scalar iso-surface at a concentration m times the local standard deviation above the local mean, for $x = 3$ (○), 5 (△), and 7 (▽), at $x = 40\,H$; for $D_{nozzle} = 4.7$ mm and $Re = 10\,000$. (*b*) Coverage length underestimate for the fBm objects at dimensions $D \approx 1.0$ (——), 1.1046 (– – –), and 1.2553 (– · · –).

The coverage length underestimate is essentially the ratio of the total iso-surface length to the length as it appears at a larger scale. This measure is useful because the coverage length underestimate shows universal characteristics similar to the coverage dimension, and hence could be employed to correct under-resolved estimates of the coverage length. The derivation in the Appendix shows that the coverage length underestimate at a given scale is a function of the coverage dimension at smaller scales.

Figure 13(*a*) shows the coverage length underestimate for three thresholds. The coverage length underestimate appears independent of the threshold level in the viscous–convective range with the individual curves deviating at and above the Kolmogorov length scale. We evaluated the coverage length underestimate for fBm sets with coverage dimension in the same range as the turbulent iso-surface data, and figure 13(*b*) reveals that the underestimate increases rapidly with increasing scale for all three object sets. Whereas the length of the passive scalar iso-surfaces may be at most incorrect by a factor of 2, the length estimation may be underestimated by a much larger factor at coarse scales for the fBm sets. The comparison again demonstrates the unique characteristics of the turbulent iso-surface data compared to random synthetic objects. For the turbulent iso-surface data, the trends with downstream distance, Reynolds number and nozzle diameter are similar to those reported above for the coverage dimension. In particular, the coverage length underestimate appears universal in the viscous–convective regime and demonstrates similar dependence in the inertial–convective regime as observed for the coverage dimension.

Catrakis *et al.* (2002) proposed an area–volume ratio, $\Omega_3(\lambda)$, as the ratio of the total interfacial area normalized by the volume of the bounding box to the 2/3rd power. The total interfacial area is estimated as $L_3(\lambda) = \lambda^2 N_3(\lambda)$ and the volume of the bounding box is equal to δ_b^3. This quantity is generalized to other embedding

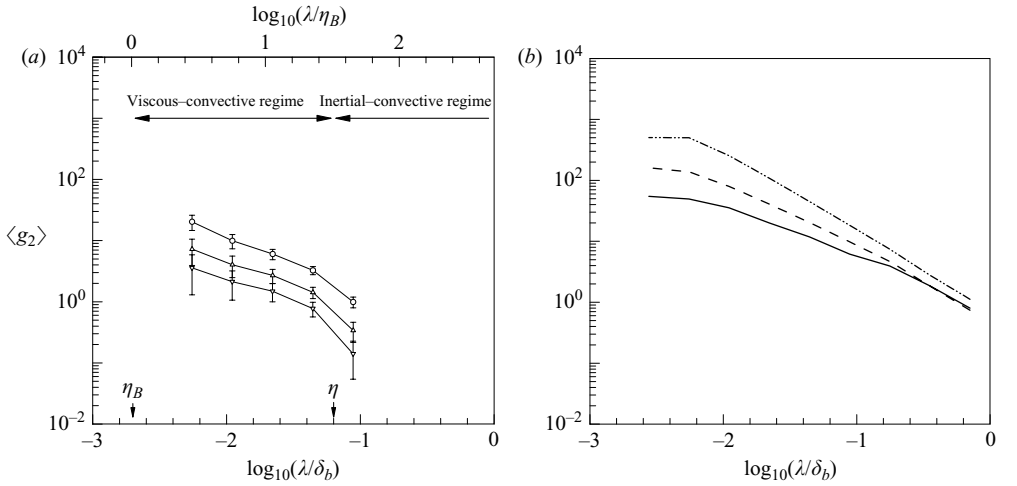

FIGURE 14. (*a*) Scale–local length–area density as a function of concentration threshold. Data plotted versus normalized scales, λ/δ_b and λ/η_B, for the passive scalar iso-surface at a concentration m times the local standard deviation above the local mean, for $m=3$ (○), 5 (△) and 7 (▽), at $x=40\,H$; for $D_{nozzle}=4.7$ mm and $Re=10\,000$. (*b*) Scale–local length–area density for the fBm objects at dimensions $D\approx 1.0$ (——), 1.1046 (– – –) and 1.2553 (–···–).

dimensions, for $d \geqslant 2$, by the following relationship:

$$\Omega_d(\lambda) = \frac{\lambda^{d_t} N_d(\lambda)}{\left(\delta_b^d\right)^{d_t/d}} = \left(\frac{\lambda}{\delta_b}\right)^{d_t} N_d(\lambda). \tag{4.4}$$

For our data the embedding dimension is $d=2$, thus this measure is interpreted as the length–area ratio and is qualitatively the same as the coverage length per bounding box area (i.e. figure 12). As described in Catrakis *et al.* (2002) (for $d=3$), the scale–local length–area density, $g_d(\lambda) = -\mathrm{d}\Omega_d(\lambda)/\mathrm{d}\lambda$, and its exponent, $\alpha_g(\lambda)$, are the slope of the scale–cumulative length–area ratio curve and the logarithmic derivative of the scale-local length–area density, respectively. $g_2(\lambda)$ is interpreted as the contribution to $\Omega_2(\lambda)$ from the local features of the object structure at scale λ.

Note that $g_2(\lambda)$ is negative when the coverage dimension is less than the topological dimension, which occurs for the scalar field in the present study owing to the intermittency or 'spottiness' of the fields at larger scales. The significance of $\alpha_g(\lambda)$ is that it corresponds to the local fractal dimension of the structure at the scale λ and is a better measure (than coverage dimension) to detect self-similarity of turbulent iso-surface structure in the inertial–convective regime (Catrakis *et al.* 2002). Catrakis *et al.* (2002) reported that the 'fractal dimension at the local scale' was constant at $\alpha_g = 1.3$ in a narrow range of scales that correspond to the inertial–convective regime.

Figure 14(*a*) shows the scale–local length–area density for three concentration thresholds. The scale–local contribution to the scale–cumulative length–area ratio is dominated by complexity in the viscous–convective regime, and the contribution decreases with increasing scale. Above the Kolmogorov length scale ($\log_{10}(\lambda/\delta_b)\approx -1.2$), the contributions for the higher thresholds are negative because of the coverage dimension falling below the topological dimension (see figure 8). These negative data points are not shown in the logarithmic plot. Overall, $\langle g_2(\lambda)\rangle$ decreases with increasing threshold. For the fBm sets, $\langle g_2(\lambda)\rangle$ decreases with increasing scale and approaches a power law decay consistent with the behaviour of a self-similar

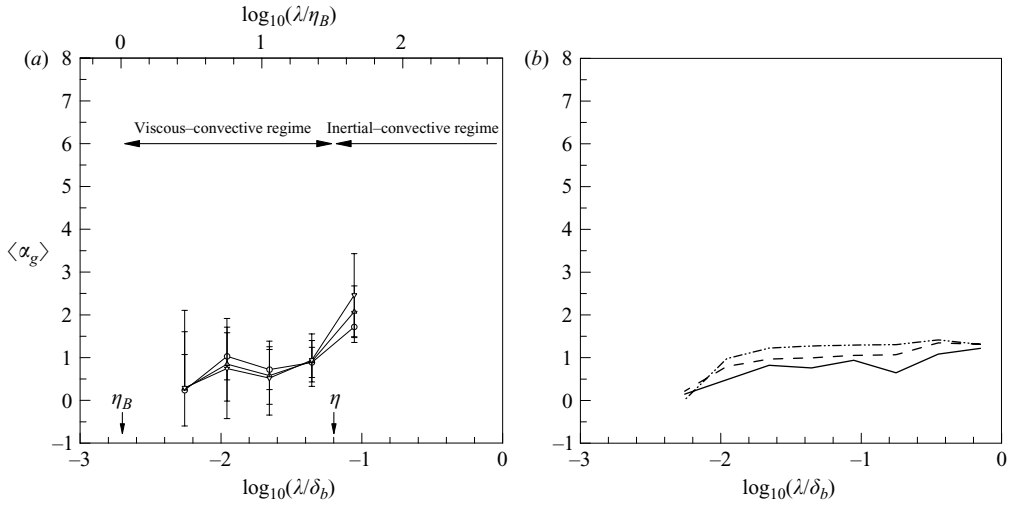

FIGURE 15. (*a*) Scale–local length–area density exponent as a function of concentration threshold. Data plotted versus normalized scales, λ/δ_b and λ/η_B, for the passive scalar iso-surface at a concentration m times the local standard deviation above the local mean, for $m = 3$ (○), 5 (△) and 7 (▽), at $x = 40\,H$; for $D_{nozzle} = 4.7$ mm and $Re = 10\,000$. (*b*) Scale–local length–area density exponent for the fBm objects at dimensions $D \approx 1.0$ (——), 1.1046 (– – –) and 1.2553 (–·–·–).

fractal (figure 14*b*). Hence, the contribution at scales larger than the Kolmogorov scales for the fBm sets particularly contrasts with the contribution for the turbulent iso-surfaces.

Figure 15(*a*) shows the exponent $\langle\alpha_g(\lambda)\rangle$ for three threshold values. Catrakis *et al.* (2002) did not define $\alpha_g(\lambda)$ for coverage dimensions less than the topological dimension. As a result, for the data shown in figure 15(*a*) the higher threshold levels yield undefined $\langle\alpha_g(\lambda)\rangle$ in the inertial–convective regime. However, $\langle\alpha_g(\lambda)\rangle$ fluctuates around a value of approximately 0.8 in the viscous–convective regime. We note here that plots (not shown) of $\langle\alpha_g(\lambda)\rangle$ variation with downstream distance, Reynolds number, and nozzle diameter do not indicate self-similarity in the inertial–convective regime (i.e. for $\log_{10}(\lambda/\delta_b) > -1.2$). The only range where the exponent is close to a constant value is in the viscous–convective range. Further, the constant appears to decrease with increase in Reynolds number. Although Catrakis *et al.* (2002) reported a constant value of 1.3, it is clear from the current data that this value is not universal. Figure 15(*b*) shows the exponent $\langle\alpha_g(\lambda)\rangle$ for the fBm sets approaching a constant value that depends on the fractal dimension of the objects, which is again consistent with a self-similar behaviour. The results again strongly contrast with the turbulent iso-surface data for larger scales.

5. Lacunarity

Mandelbrot (1983) presented the measure of lacunarity to address the elusive notion of texture by quantifying the deviation of an object from translational invariance. Lacunarity distinguishes objects that have the same fractal dimension, but different levels of regularity or homogeneity. Plotnick *et al.* (1996), among others, used lacunarity to describe patterns occurring in several examples in natural systems. Lacunarity has considerable significance from the point of view of turbulent mixing

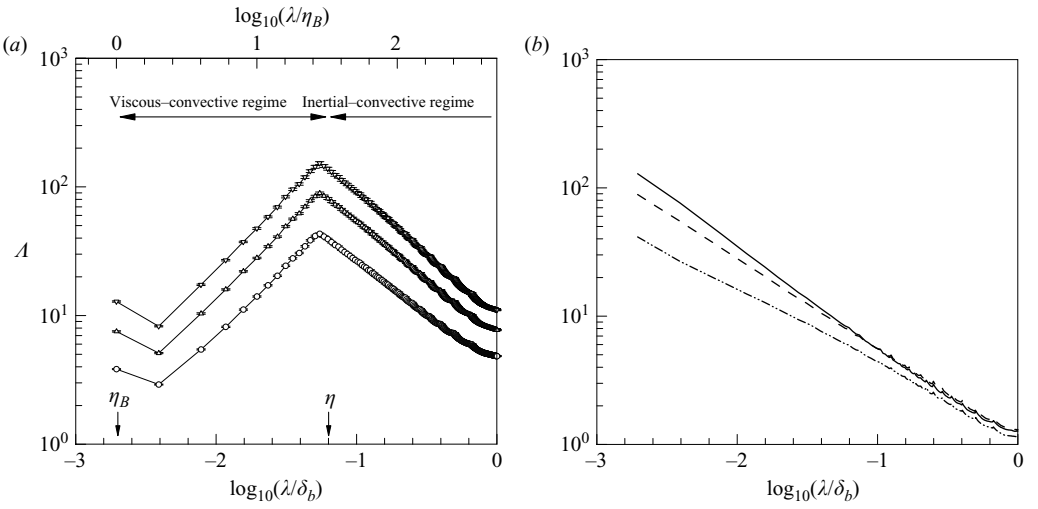

FIGURE 16. (*a*) Lacunarity as a function of concentration threshold. Data plotted versus normalized scales, λ/δ_b and λ/η_B, for the passive scalar iso-surface at a concentration m times the local standard deviation above the local mean, for $m = 3$ (○), 5 (△) and 7 (▽), at $x = 40\,H$; for $D_{nozzle} = 4.7$ mm and $Re = 10\,000$. (*b*) Lacunarity for the fBm objects at dimensions $D \approx 1.0$ (——), 1.1046 (– – –) and 1.2553 (– · · –).

of passive scalars. For instance, lacunarity is a sensitive measure of deviation from local homogeneity, in contrast to the scaling regimes in the spectra that assume local statistical homogeneity. In this section, we examine the lacunarity of the concentration iso-surfaces in order to describe the homogeneity of the extracted surfaces. As described below, lacunarity is readily calculated as a function of scale.

Lacunarity is defined as the ratio of the second moment to the square of the average of the spatial mass-distribution function of any set (Allain & Cloitre 1991) and is not directly related to the coverage count. The gliding-box algorithm is used to generate the mass distribution function for a given scale size, λ. In this algorithm, a box of size λ glides across the set, sequentially residing in all possible positions. The number of pixels in the gliding box that contain any part of the iso-surface is defined as the mass of the gliding box. As the gliding box takes all possible positions in the bounding box, the mass fluctuates according to the spatial distribution of the set. The PDF of these fluctuations is the mass-distribution at scale size λ, $pdf_\lambda(m)$. The lacunarity at scale size λ is thus defined as:

$$\Lambda(\lambda) = \frac{\displaystyle\int_{m=0}^{\infty} m^2\, pdf_\lambda(m)\,\mathrm{d}m}{\left(\displaystyle\int_{m=0}^{\infty} m\;\, pdf_\lambda(m)\mathrm{d}m\right)^2} = 1 + \frac{\sigma_m^2}{\mu_m^2}, \tag{5.1}$$

where σ_m^2 is the variance and μ_m is the mean of the mass-distribution function. A lacunarity value of 1 indicates homogeneity, whereas larger values indicate spatial in-homogeneity.

Figure 16(*a*) shows the lacunarity function for three concentration thresholds. From the minimum value at scales just larger than the Batchelor-scale, the lacunarity increases with increasing scale through the viscous–convective regime. For scales larger than the Kolmogorov length scale, the lacunarity decreases. Increasing lacunarity

corresponds to increasingly patchy structure, therefore it can be concluded that the iso-surfaces viewed at the viscous–convective scales are highly irregular and decrease in homogeneity with increasing scale up to the Kolmogorov length scale. The figure also shows that the structure is most inhomogenous around the Kolmogorov length scale. In contrast, the behaviour of lacunarity for the fBm objects (figure 16*b*) appears as a monotonic power law decay with increasing scale. Again, this demonstrates the unique characteristics of the turbulent iso-surface data compared to that of random synthetic objects. Overall, the lacunarity (and inhomogeneity) increases with increasing concentration threshold (figure 16*a*). Further, the steepness of the decrease in lacunarity in the inertial–convective range increases with threshold. The lacunarity curves qualitatively were similar for the cases of varying downstream distance, Reynolds number and nozzle diameter. We note that lacunarity was observed to increase with downstream distance for all three threshold levels, indicating an increasingly inhomogeneous field with downstream distance. Also the lacunarity decreased with increasing Reynolds number and nozzle diameter suggesting a more homogeneous field at higher Reynolds number and larger source diameter.

6. Conclusions

Passive scalar iso-surfaces were analysed by the box-counting algorithm to generate scale-dependent coverage statistics of the iso-surfaces including the coverage dimension. These results have been compared to the coverage statistics of simulated iso-surfaces represented by fractional Brownian motion. The fractal measures of the passive scalar iso-surfaces were found to be scale dependent with level 3 complexity and clearly do not resemble the fractal characteristics of fBm sets in agreement with Frederiksen *et al.* (1997). Based on our data, we find that the coverage dimension varies with scale in a universal form in the viscous–convective range. The coverage length underestimate reflects this universal behaviour and forms an important measure for practical applications. Specifically, we may estimate the true interfacial length based on the variation of the coverage length underestimate in the viscous–convective regime. Estimating the interfacial length is important in many applications such as reactive and non-reactive mixing, aero-optics and aero-acoustics. The universal behaviour in this context relates to the common trends observed with varying Reynolds number, source nozzle size, concentration threshold of the iso-surface, distance from the source, and local mean scalar gradient. Additional data and comparisons are required in order to evaluate whether these trends are more broadly universal. The lacunarity of the iso-surfaces increases with scale in the viscous–convective regime, which suggests increasing inhomogeneity. The fluctuating iso-surfaces appear to be most inhomogeneous around the Kolmogorov length scale shown by the local maximum of lacunarity.

The authors gratefully acknowledge the financial support of the National Science Foundation (CTS-0303406).

Appendix. Derivation of the coverage length underestimate

The coverage length underestimate and coverage dimension are connected by the following relationships. The scale–local area–volume density is defined as (Catrikis

et al. 2002):

$$g_d(\lambda) \equiv -\frac{\mathrm{d}\Omega_d(\lambda)}{\mathrm{d}\lambda} = \frac{\Omega_d(\lambda)}{\lambda}(D_d(\lambda) - d_t), \tag{A 1}$$

where $\Omega_d(\lambda)$ is the scale–cumulative area–volume ratio. Divide (A 1) by $\Omega_{d,tot}$ to yield:

$$-\frac{\mathrm{d}}{\mathrm{d}\lambda}\left(\frac{\Omega_d(\lambda)}{\Omega_{d,tot}}\right) = \frac{\Omega_d(\lambda)}{\Omega_{d,tot}}\frac{(D_d(\lambda) - d_t)}{\lambda}. \tag{A 2}$$

Observe that the coverage length underestimate is related to the area–volume ratio as:

$$L_{d,u} \equiv \frac{L_{d,tot}}{L_d} = \left(\frac{\lambda^{d_t}}{\lambda^{d_t}}\right)\frac{N_{d,tot}}{N_d} = \left(\frac{\lambda^{d_t}/\delta_b}{\lambda^{d_t}/\delta_b}\right)\frac{N_{d,tot}}{N_d} = \frac{\Omega_{d,tot}}{\Omega_d} \tag{A 3}$$

and substitute to yield:

$$\frac{1}{L_{d,u}}\frac{\mathrm{d}}{\mathrm{d}\lambda}(L_{d,u}) = \frac{(D_d(\lambda) - d_t)}{\lambda}. \tag{A 4}$$

Integrate over the interval 0 to λ to produce the relationship between the coverage length underestimate and coverage dimension:

$$\ln(L_{d,u}(\lambda)) - \ln(L_{d,u}(0)) = \int_0^{\lambda} \frac{1}{\tilde{\lambda}}(D_d(\tilde{\lambda}) - d_t)\,\mathrm{d}\tilde{\lambda} \tag{A 5}$$

$$L_{d,u}(\lambda) = \exp\left(\int_0^{\lambda} \frac{1}{\tilde{\lambda}}(D_d(\tilde{\lambda}) - d_t)\,\mathrm{d}\tilde{\lambda}\right) \tag{A 6}$$

Equation (A 6) is integrable in the given limits as $g_d(\lambda \to 0) = 0$ (Catrakis *et al.* 2002). From (A 6), it is clear that a universal variation of the coverage dimension in the viscous–convective regime corresponds with universal behaviour of the coverage length underestimate. The practical usefulness is that the coverage length underestimate can be employed to correct under-resolved estimates of the coverage length.

REFERENCES

Allain, C. & Cloitre, M. 1991 Characterizing the lacunarity of random and deterministic fractal sets. *Phys. Rev.* A **44**, 3352–3358.

Catrakis, H. J. 2000 Distribution of scales in turbulence. *Phys. Rev.* E **62**, 564–578.

Catrakis, H. J. & Bond, C. L. 2000 Scale distributions of fluid interfaces in turbulence. *Phys. Fluids* **12**, 2295–2301.

Catrakis, H. J. & Dimotakis, P. E. 1996 Mixing in turbulent jets: scalar measures and isosurface geometry. *J. Fluid Mech.* **317**, 369–406.

Catrakis, H. J. & Dimotakis, P. E. 1998 Shape complexity in turbulence. *Phys. Rev. Lett.* **80**, 968–971.

Catrakis, H. J., Aguirre, R. C. & Ruiz-Plancarte, J. 2002 Area–volume properties of fluid interfaces in turbulence: scale-local self-similarity and cumulative scale dependence. *J. Fluid Mech.* **462**, 245–254.

Crimaldi, J. P. & Koseff, J. R. 2001 High-resolution measurements of the spatial and temporal scalar structure of a turbulent plume. *Exps. Fluids* **31**, 90–102.

Crimaldi, J. P., Wiley, M. B. & Koseff, J. R. 2002 The relationship between mean and instantaneous structure in turbulent passive scalar plumes. *J. Turbulence* **3**(014), 1–24.

Dasi, L. P. 2004 The small-scale structure of passive scalar mixing in turbulent boundary layers. PhD thesis, Georgia Institute of Technology.

Dimotakis, P. E. 2000 The mixing transition in turbulent flows. *J. Fluid Mech.* **409**, 69–98.

Fackrell, J. E. & Robins, A. G. 1982 Concentration fluctuations and fluxes in plumes from point sources in a turbulent boundary layer. *J. Fluid Mech.* **117**, 1–26.

Ferrier, A. J., Funk, D. R. & Roberts, P. J. W. 1993 Application of optical techniques to the study of plumes in stratified fluids. *Dyn. Atmos. Oceans* **20**, 155–183.

Fitzgerald, E. J. & Jumper, E. J. 2004 The optical distortion mechanism in a nearly incompressible free shear layer. *J. Fluid Mech.* **512**, 153–189.

Frederiksen, R. D., Dahm, W. J. A. & Dowling, D. R. 1996 Experimental assessment of fractal scale-similarity in turbulent flows. Part 1. One-dimensional intersections. *J. Fluid Mech.* **327**, 35–72.

Frederiksen, R. D., Dahm, W. J. A. & Dowling, D. R. 1997 Experimental assessment of fractal scale-similarity in turbulent flows. Part 2. Higher-dimensional intersections and non-fractal inclusions. *J. Fluid Mech.* **338**, 89–126.

Freund, J. B. 2001 Noise sources in a low-Reynolds-number turbulent jet at Mach 0.9. *J. Fluid Mech.* **438**, 277–305.

Lück, St., Renner, Ch., Peinke, J. & Friedrich, R. 2006 The Markov–Einstein coherence length – a new meaning for the Taylor length in turbulence. *Phys. Lett.* A **359**, 335–338.

Mandelbrot, B. B. 1975 On the geometry of homogeneous turbulence, with stress on the fractal dimension of the iso-surfaces of scalars. *J. Fluid Mech.* **72**, 401–416.

Mandelbrot, B. B. 1983 *The Fractal Geometry of Nature*. Freeman, New York.

Miller, P. L. & Dimotakis, P. E. 1991 Stochastic geometric-properties of scalar interfaces in turbulent jets. *Phys. Fluids* A **3**, 168–177.

Peitgen, H.-O., Jürgens, H. & Saupe, D. 1992 *Chaos and Fractals: New Frontiers of Science*. Springer.

Plotnick, R. E., Gardner, R. H., Hargrove, W. W., Prestegaard, K. & Perlmutter, M. 1996 Lacunarity analysis: a general technique for the analysis of spatial patterns. *Phys. Rev.* E **53**, 5461–5468.

Pope, S. B. 1988 The evolution of surfaces in turbulence. *Intl J. Engng Sci.* **26**, 445–469.

Prasad, R. R. & Sreenivasan, K. R. 1990 Quantitative three-dimensional imaging and the structure of passive scalar fields in fully turbulent flows. *J. Fluid Mech.* **216**, 1–34.

Schuerg, F. 2003 Fractal geometry of iso-surfaces of a passive scalar in a turbulent boundary layer. MS thesis, Georgia Institute of Technology.

Schumacher, J. & Sreenivasan, K. R. 2005 Statistics and geometry of passive scalars in turbulence. *Phys. Fluids* **17**, 125107.

Shepherd, I. G., Cheng, R. K. & Talbot, L. 1992 Experimental criteria for the determination of fractal parameters of premixed turbulent flames. *Exps. Fluids* **13**, 386–392.

Spalart, P. R. 1988 Direct simulation of a turbulent boundary-layer up to $Re_\theta = 1410$. *J. Fluid Mech.* **187**, 61–98.

Sreenivasan, K. R. 1991 Fractals and multifractals in fluid turbulence. *Annu. Rev. Fluid Mech.* **23**, 539–600.

Sreenivasan, K. R. & Meneveau, C. 1986 The fractal facets of turbulence. *J. Fluid Mech.* **173**, 357–386.

Sreenivasan, K. R., Prasad, R. R., Meneveau, C. & Ramshankar, R. 1989 The fractal geometry of interfaces and the multifractal distribution of dissipation in fully turbulent flows. *Pure Appl. Geophys.* **131**, 43–60.

Tachie, M. F., Balachandar, R. & Bergstrom, D. J. 2003 Low Reynolds number effects in open-channel turbulent boundary layers. *Exps. Fluids* **34**, 616–624.

Villermaux, E. & Innocenti, C. 1999 On the geometry of turbulent mixing. *J. Fluid Mech.* **393**, 123–147.

Villermaux, E., Innocenti, C. & Duplat, J. 2001 Short circuits in the Corrsin–Obukhov cascade. *Phys. Fluids* **13**, 284–289.

Webster, D. R., Rahman, S. & Dasi, L. P. 2003 Laser-induced fluorescence measurements of a turbulent plume. *J. Engng Mech.* **129**, 1130–1137.

Welander, P. 1955 Studies on the general development of motion in a two-dimensional, ideal fluid. *Tellus* **7**, 141–156.